Journal of Materials Chemistry C

Accepted Manuscript

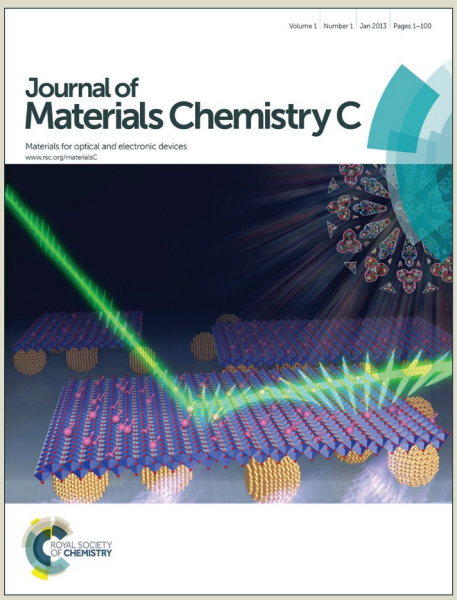

ROYAL SOCIETY OF CHEMISTRY

www.rsc.org/materialsC

Journal Name

RSCPublishing

ARTICLE

Phase transition and piezoelectricity of sol-gel-processed Sm-doped $BiFeO_3$ thin films on $Pt(111)/Ti/SiO_2/Si$ substrates

Wei Sun, Jing-Feng Li*, Qi Yu and Li-Qian Cheng

Cite this: DOI: 10.1039/x0xx00000x

Received 00th January 2012,
Accepted 00th January 2012

DOI: 10.1039/x0xx00000x

www.rsc.org/

$Bi_{1-x}Sm_xFeO_3$ thin films (x=0, 0.05, 0.10 and 0.15) on $Pt(111)/Ti/SiO_2/Si$ substrates were fabricated by the sol-gel process and the effect of Sm doping on their crystal structure was studied by synchrotron radiation X-ray diffraction and Raman spectroscopy. It is revealed that a phase transition from rhombohedral to orthorhombic structure takes place with increasing Sm content, resulting in two-phase coexistence at x=0.10, where the two phases are *R*3*c* and *Pbam* according to the refinement result. The phase transition can be ascribed to the difference between the smaller radius of Sm^{3+} than its substituted Bi^{3+}. Meanwhile, the composition-dependent dielectric, ferroelectric and piezoelectric properties were also investigated. PFM scanning and switching spectroscopy results confirmed the enhancement of piezoresponse at x=0.10 corresponding to the rhombohedral-orthorhombic morphotropic phase boundary (MPB) region. The ferroelectric properties of Sm-doped $BiFeO_3$ films were found to decrease with increasing Sm content, indicating that the extrinsic piezoelectric response contributes more to the improved piezoelectricity at the MPB.

1 Introduction

Bismuth ferrite ($BiFeO_3$) is a room-temperature multiferroic material exhibiting ferroelectricity with a high Curie temperature (T_C~1103K) and anti-ferromagnetism with a high Neel temperature (T_N~673K).[1] At room temperature, $BiFeO_3$ possesses a rhombohedrally distorted perovskite structure with spontaneous polarization directions along the $<111>_{pc}$ diagonals. The remnant polarization can be as high as ~100μC/cm^2, making it a promising material for the data storage applications.[2, 3] Zeches *et al*. found that $BiFeO_3$ grown epitaxially on $LaAlO_3$ substrate with 4.3% compressive strain could demonstrate the coexistence of rhombohedral (*R*) and tetragonal (*T*) phases with a remarkable enhancement of piezoresponse,[4] which is similar to the morphotropic phase boundary (MPB) in $Pb(Zr,Ti)O_3$ and related systems.[5, 6] This work shed light on the potential piezoelectric use of $BiFeO_3$ thin films for sensors and energy harvesters in microelectromechanical systems (MEMS), thus bringing another interesting topic on this material.[7] Besides, $BiFeO_3$ is lead-free and environmentally friendly, which has also aroused considerable interests worldwide.

In 2008, Takeuchi *et al.* proposed another rhombohedral-orthorhombic (*R*-*O*) MPB that was induced by A-site doping with 14% Sm in $BiFeO_3$ films grown on $SrTiO_3$, whose piezoelectric coefficient d_{33} could reach 110 pm/V.[8-10] Thereafter, many studies have been devoted to $BiFeO_3$ thin films doped with rare-earth elements. Most of the studies concerning about the piezoelectric performance were based on $BiFeO_3$ thin films fabricated on the single-crystalline substrates like $LaAlO_3$ and $SrTiO_3$ by pulse laser deposition,[11-18] and some focused on the ceramic or nanoparticle.[19-22] While for $BiFeO_3$ thin films grown on silicon wafers which are widely used in microelectronic devices, the studies were mainly focused on the ferroelectricity or magnetoelectricity.[23-31] Very limited amount of studies have be devoted to its piezoelectric property, especially using piezoresponse force microscopy (PFM) which has been proven to be a powerful technique in the piezoelectric study.

In this work, a series of Sm-doped $BiFeO_3$ thin films was prepared on $Pt(111)/Ti/SiO_2/Si$ substrate by a sol-gel method. Their composition-dependent dielectric and ferroelectric properties were studied. PFM was employed to investigate the piezoelectric property and domain characteristics with an emphasis on the effect of Sm contents on the phase evolution. The crystal structure was found to change from rhombohedral to orthorhombic phase with increasing Sm content, and the coexistence of *R*3*c* and *Pbam* phases were considered to be the origin of the enhanced piezoresponse at the composition of $Bi_{0.90}Sm_{0.10}FeO_3$, where the potential MPB located.

2 Experimental

Synthesis

The experiments for film preparation used bismuth nitrate [$Bi(NO_3)_3{\cdot}5H_2O$] (99.99%), samarium nitrate [$Sm(NO_3)_3{\cdot}6H_2O$] (99.9%) and iron nitrate [$Fe(NO_3)_3{\cdot}9H_2O$] (99.99%) as starting materials, which were dissolved in 2-mothoyethanol (2-MOE) solvent. Citric acid (99.995%) was then added as the chelating agent.

7% excessive Bi was added to compensate for its volatilization during heat treatment. The mixed solutions were stirred continuously for 4 h and aged for 72 h, and the resultant solutions were then deposited onto Pt(111)/Ti/SiO_2/Si substrates by spin coating at 5000 rpm for 30 s in the ambient atmosphere. After deposition of each layer, the films were pyrolyzed at 380 °C to remove organics and annealed at 550 °C for crystallization. The deposition-pyrolysis-crystallization process was repeated for 10 times to reach a desired thickness of ~400 nm.

Characterization

The crystallographic structure of thin films was analysed by X-ray diffraction (XRD, D/max-RB, Rigaku, Japan) using Cu-K_α radiation (λ=1.5418 Å). Step scanning was performed by employing synchrotron radiation (BL14B1, SSRF) with λ=1.2398Å. The data were further analysed via the Rietveld refinement using Maud software. Raman spectrum was performed on a Raman spectrometer (RM2000, Renishaw, UK) with a radiation of Ar^+ laser at 532 nm. The cross-section morphology was observed via a field-emission scanning electron microscope (FE-SEM, LEO1530, Germany). The surface morphology and piezoelectric response were characterized using an atomic force microscope (AFM, MFP-3D, Asylum Research, USA) with a functionality of piezoresponse force microscope (PFM) for the local polarization detection and switching spectroscopy. A Pt-coated cantilever (Olympus AC240, nominal spring constant 2 N/m, resonant frequency 70 kHz) was used with the platinized silicon substrates as the counter electrodes. The dielectric and ferroelectric measurements were performed using impedance analyzer (4294A, Agilent, USA) and ferroelectric tester (Multiferroic, Radiant Technology, USA) respectively. For the ferroelectric test, Pt top electrodes (100 nm in thickness and 400 μm in diameter) were sputter-deposited onto the film surface through a shadow mask.

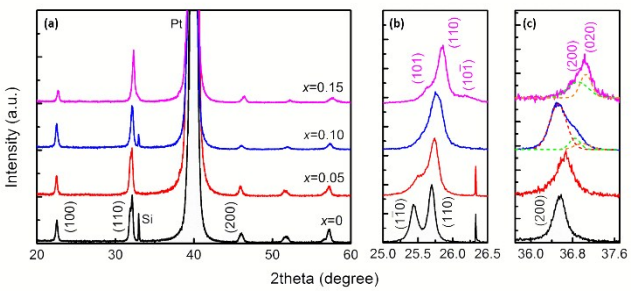

Fig. 1. XRD patterns of $Bi_{1-x}Sm_xFeO_3$ thin films synthesized on Pt(111)/Ti/SiO_2/Si substrate: (a) wide range scanning using Cu-K_α radiation; (b) step scanning of $\{110\}_{pc}$ peaks using synchrotron radiation; (c) step scanning of $\{200\}_{pc}$ peaks using synchrotron radiation.

3 Results and discussion

Microstructure and phase evolution

Fig. 1(a) shows the XRD patterns of the $BiFeO_3$ thin films with different Sm contents. The diffraction peaks are indexed according to a pseducubic phase in order to display the structure evolution clearly. By matching the detected peaks with the standard PDF card of $BiFeO_3$ (PDF#72-2112), no secondary phase was found and peak intensity distribution of all peaks suggests a polycrystalline feature. The (111) and (11-1) peaks of $Bi_{1-x}Sm_xFeO_3$ are overlapped by the (111) peak of Pt bottom electrode. Figs. 1(b) and 1(c) are the step scanning results of {110} and {200} peaks obtained by synchrotron radiation, respectively. The high intensity and monochromaticity of synchrotron X-ray source allow for high resolution of the diffraction pattern, which provides more reliable information for structural analysis. It can be seen that the (110) and (1-10) peaks are clearly separated and only one (200) peak was found for the undoped $BiFeO_3$ sample, corresponding to a rhombohedral cell ($a=b=c$ and $\alpha<90^o$). At x=0.05, the phase structure is still rhombohedral, but the (110) and (1-10) peaks get closer, indicating that the lattice angle α approaches to 90°. Besides, the peaks of $Bi_{0.95}Sm_{0.05}FeO_3$ sample shift towards higher angle side compared with undoped $BiFeO_3$, which can be attributed to the decreased d space induced by smaller radius of Sm^{3+} (1.098Å) than Bi^{3+} (1.17Å). At x=0.15, {110} splits into three peaks, corresponding to (101), (110) and (10-1) respectively, and {200} consists of two peaks: (200) and (020) displayed in dash lines in green and orange respectively. The splitting of {110} and {200} indicates a typical orthorhombic phase or the so-called monoclinic one in which $a=c>b$, and $\alpha=\gamma=90^o$, $\beta<90^o$.[19-21] To distinguish the *O* phase from *R*, the peaks are indexed in pink. The diffraction pattern is in good agreement with literatures, which reported that 15% Sm doping resulted in an orthorhombic phase.[11, 19] When x=0.10, the (110) peak shows no apparent splitting, but an asymmetry is found with left side bulged. Meanwhile, broadening {200} peaks with a shoulder peak on the right side manifest distinct difference from other compositions, suggesting that there may be two phases in the film. According to peak-differentiate results, the {200} diffraction signal can be regarded as the combination of (200) peak (red dash line) of *R* phase and (200) + (020) peaks (green and orange dash lines) of *O* phase, which suggests that both *R* and *O* phases exist in this composition. To further assure the structure of the compositions, XRD patterns were analysed with Rietveld refinement and detailed refinement results can be found in the supplementary materials.[32] It is revealed that for x=0 and 0.05, the patterns fit well with *R*3*c* structure. According to fitting factors, the refinement of x=0.10 matches well with *R*3*c* (68.55%) + *Pbam* (31.45%), confirming the the coexistence of *R* and *O* phases. For the refinement of x=0.15, *Pbam* (10.15%) + *Pnma* (89.85%) combination gave the smallest fitting factors. The result shows that there are two different *O* phases in this composition, of which *Pbam* is a $PbZrO_3$-type anti-polar phase while *Pnma* is a centrosymmetric phase.[33,34]

Raman spectroscopy was further used to study the detailed changes of crystal structure in Sm-doped $BiFeO_3$ thin films. Fig. 2 shows the Raman spectra of $Bi_{1-x}Sm_xFeO_3$ thin films with different Sm contents. For $BiFeO_3$ with rhombohedral phase, Raman active modes can be written as $\Gamma=4A_g+9E_g$, just like rhombohedrally distorted perovskite $LaAlO_3$ and $LaMnO_3$.[3, 35] When x=0, 0.05 and 0.10, the typical active vibration modes of A_g-1 (at c.a. 130cm^{-1}),

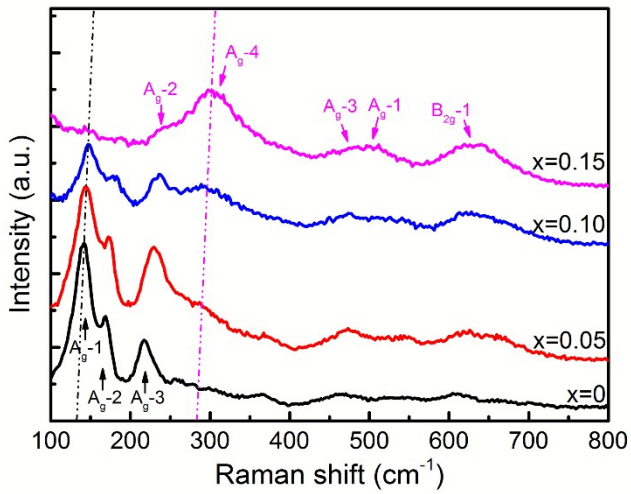

Fig. 2. Raman spectra of $Bi_{1-x}Sm_xFeO_3$ thin films.

A_g-2 (at c.a. 170cm^{-1}) and A_g-3 (at c.a. 220cm^{-1}) peaks are of high intensity that can be easily identified and are marked with black arrows in the figure. The Raman vibration frequency is related with bonding energy.[36] Since the radius of Sm^{3+} is small, the bonding energy of Sm-O is stronger than Bi-O, leading to the shift of Raman peaks towards higher wave number as the Sm content increases from 0 to 10%, as indicated by the black dash line. For x=0.15 thin film, its Raman spectrum shows a significant difference with undoped $BiFeO_3$. It is similar to orthorhombic perovskite structure like $LaMnO_3$ and $YMnO_3$ belonging to space group *Pnma*, whose Raman active mode can be written as $\Gamma=7A_g+5B_{1g}+7B_{2g}+5B_{3g}$.[37] Some strong peaks including A_g-2(at c.a. 240 cm^{-1}), A_g-4(at c.a. 300 cm^{-1}), A_g-3(at c.a. 480 cm^{-1}), A_g-1(at c.a. 500 cm^{-1}) and B_{2g}-1(at c.a. 620 cm^{-1}) are labelled in pink, consistent with the result reported by Iliev *et al*..[38] For x=0.10, both the A_g-1 peak of *R* and the A_g-4 peak of *O* can be identified, suggesting that *O* phase also exists in this composition. The stronger intensity of *R* phase vibration mode than *O* phase is also in good accordance with XRD pattern analysis in which *R* phase is dominant at x=0.10.

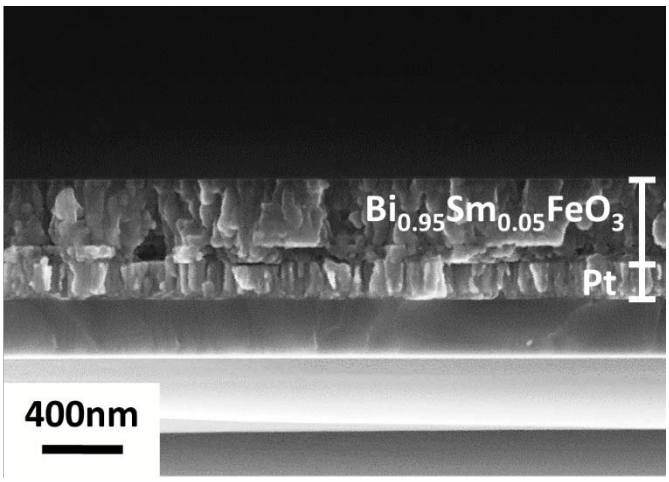

Fig. 3. Cross-sectional SEM image of $Bi_{0.95}Sm_{0.05}FeO_3$ thin film on platinized silicon substrate.

Morphology

Fig. 3 displays the cross-sectional SEM image of $Bi_{0.95}Sm_{0.05}FeO_3$ thin film as a representative and the samples with other compositions show no detectable difference. The platinum bottom electrode with column structure can be seen clearly, on which a densely grown film with a thickness of ~400 nm is well displayed. In addition, Auger Electron Spectroscopy revealed that the film was homogeneous along the depth (results are not shown here). The film has a flat surface and also shows layered structures in some regions, whose formation might be related to the layer-by-layer annealing applied in the thermal process.

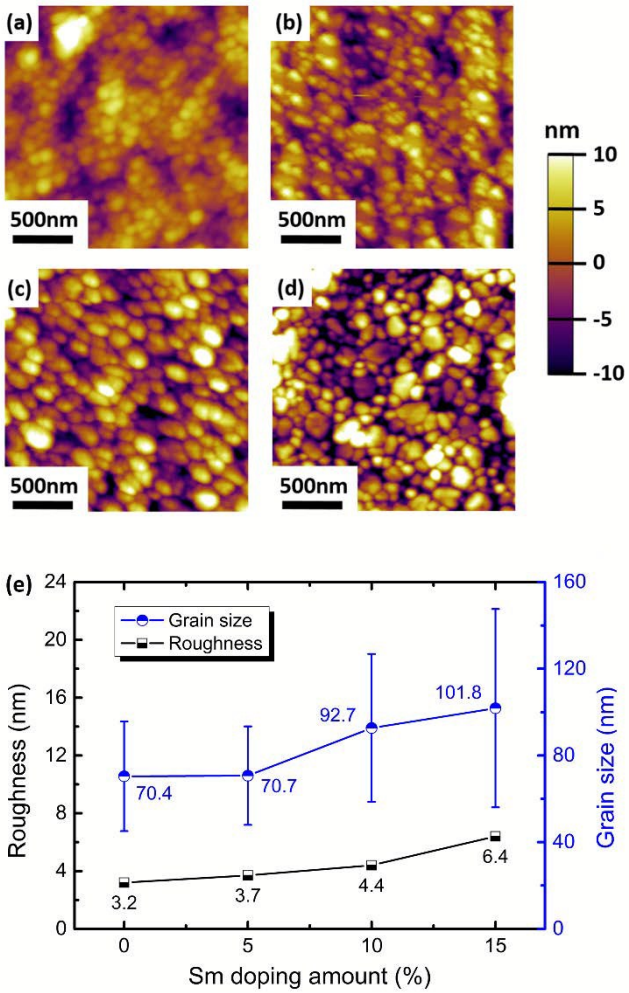

Fig. 4. (a)-(d) Surface morphology of $Bi_{1-x}Sm_xFeO_3$ thin films: (a) x=0; (b) x=0.05; (c) x=0.10; (d) x=0.15; (e) roughness and average grain size with Sm doping amount.

Figs. 4(a)-(d) are the surface morphologies by AFM of four compositions, showing a uniformly grown polycrystalline feature. The roughness values of samples are plotted in Fig. 4(e), together with the average grain sizes calculated from 100 grains randomly chosen in each graph. The error bar of grain size corresponds to the standard deviation of an average grain size. It can be seen that as Sm content increases from 0 to 15%, the roughness increases from 3.2 nm to 6.4 nm. When Sm is

5%, the grain size is comparable with pure $BiFeO_3$, which is ~70 nm. When *x* increases to 0.10 and 0.15, the average grain size increases to 92.7 nm and 101.8 nm respectively, and roughness also tends to rise slightly. A possible explanation is that Sm doping reduces the crystallization temperature of $BiFeO_3$ just like the case of La doping.[39] Since all the samples were subjected to the same thermal process and crystallized at 550 °C, one can easily envisage that grain growth may be enhanced in Sm-doped $BiFeO_3$ thin films, which should require lower thermal treatment temperatures.

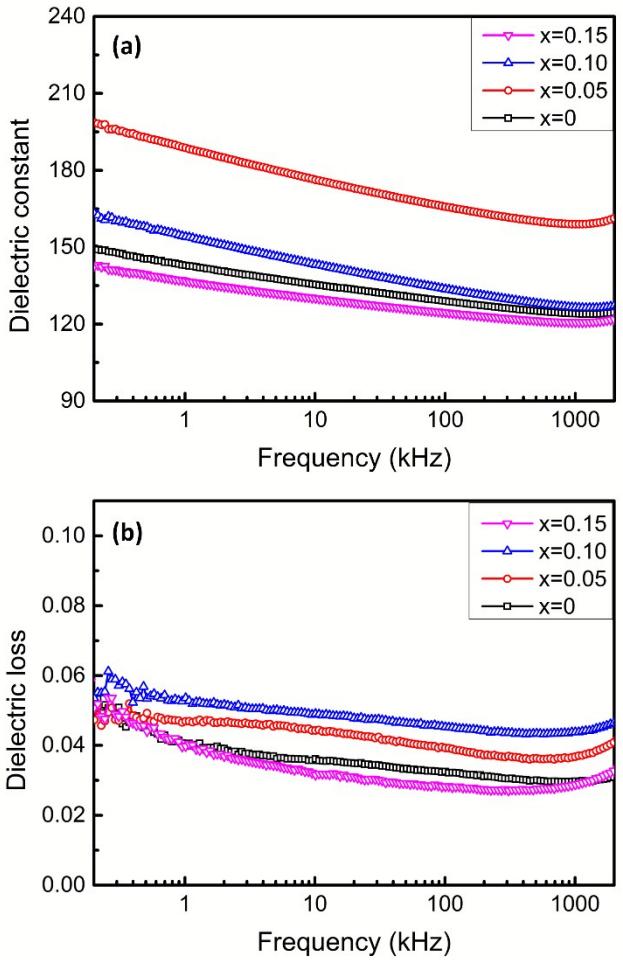

Fig. 5. Dielectric test of $Bi_{1-x}Sm_xFeO_3$ thin films: (a) dielectric constant; (b) dielectric loss.

Dielectric and ferroelectric properties

Figs. 5(a) and 5(b) display the frequency-dependent dielectric constant (ε_r) and the corresponding dielectric loss at room temperature, respectively. For all the samples, the dielectric constant decreases gradually with frequency while dielectric loss exhibits no strong frequency dependence within the tested range. The dielectric losses of four compositions are of the same order, which indicates little difference in film quality among the samples. Besides, relatively small dielectric losses suggest that the films are of high quality and low leakage, thus confirming the tested value is reliable. From Fig. 5(a), one can find that 5% Sm doping can improve the permittivity significantly, but more Sm additive leads to a decrease of dielectric constant. On one hand, dielectric constant is related to dipole moment. The improvement of dielectric constant at x=0.05 can be attributed to the substitution of Bi^{3+} with smaller Sm^{3+}, which provides larger vibration space for a larger dipole moment. The same phenomenon was also found in La-doped $BiFeO_3$ thin films.[39] On the other hand, space charges also contribute to dielectric constant, which always accumulate at grain boundaries. At x=0.05, grain size almost retains the same with undoped $BiFeO_3$, so do the amount of grain boundaries. When *x* is raised to 0.10 and 0.15, the increasing average grain size leads to a reduction of grain boundaries, which in turn decreases the dielectric constant.

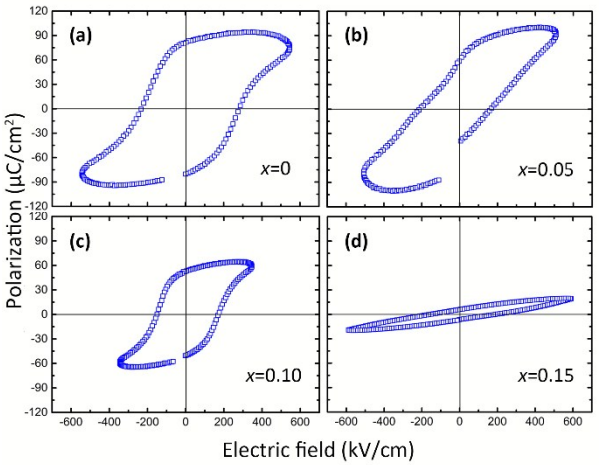

Fig. 6. Typical *P-E* hysteresis loops of $Bi_{1-x}Sm_xFeO_3$ thin films tested at 5 kHz: (a) x=0; (b) x=0.05; (c) x=0.10; (d) x=0.15.

Figs. 6(a)-(d) show the ferroelectric hysteresis loops of $Bi_{1-x}Sm_xFeO_3$ films measured at room temperature with a test frequency of 5 kHz. At x=0, P_r is 80.8 μC/cm², a value comparable with *ab* initio result and experimental one about 100 μC/cm² achieved in epitaxially grown $BiFeO_3$ thin films.[2, 11] Since the specimens prepared by chemical solution deposition is polycrystalline, grain boundaries play important roles to bring about line defects, resulting in a slight decrease of P_r compared with the previously reported value.[2, 11] For Sm-doped thin films, it is obvious that P_r and E_c decrease with increasing doping content. The decrease of P_r in x=0.05 and 0.10 samples may derive from the tendency of phase transition from *R* to *O* phase with higher degree of symmetry. At x=0.15, a significantly different *P-E* loop with a spindle shape was observed. This result shows that sufficient Sm contents in $Bi_{1-x}Sm_xFeO_3$ films could induce a *Pnma* space group, which exhibits centrosymmetry with non-piezoelectric and paraelectric behaviours.[20] Nevertheless, paraelectric phase may sometimes demonstrate non-zero P_r and E_c values as shown in Fig. 6(d) due to other effects including electrostaticity. However, we cannot exclude the possibility of weak ferroelectricity associated with the existence of a small amount of $PbZrO_3$-type *Pbam* phase as has been revealed in the refinement. The exact phase constitution in x=0.15 sample will be discussed later.

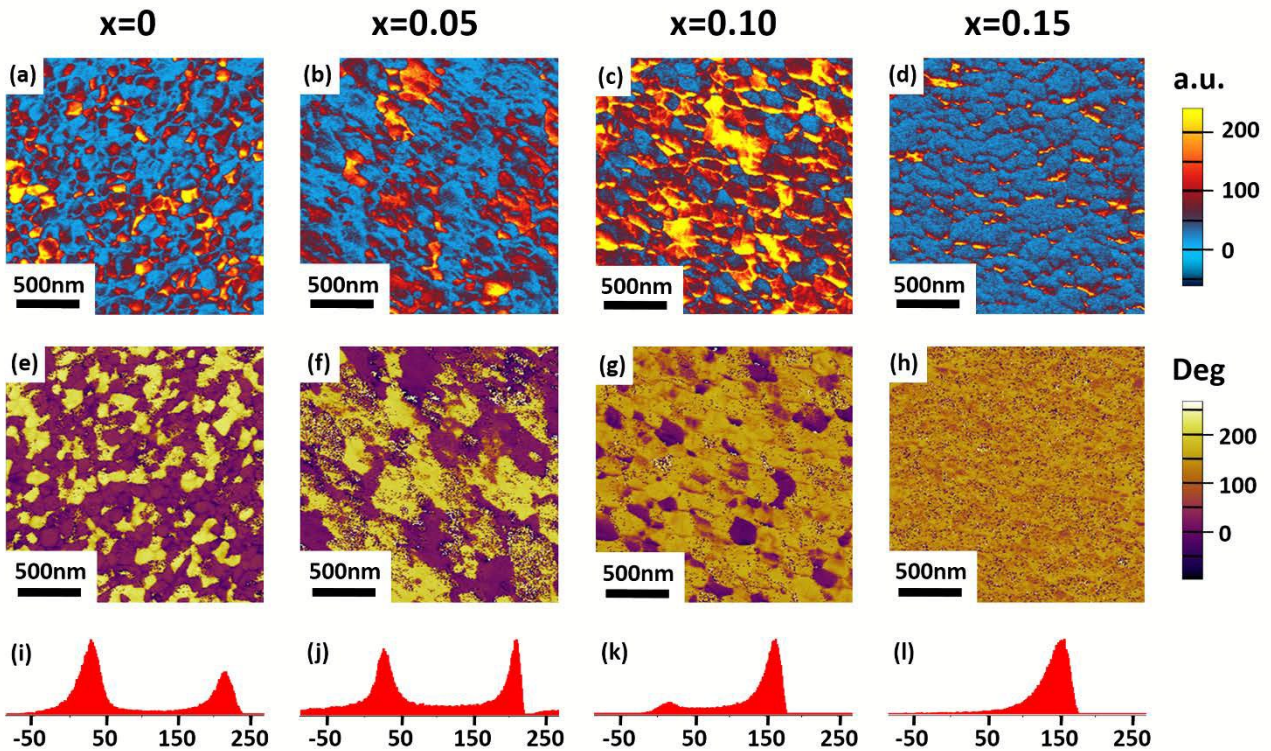

Fig. 7. Piezoresponse mappings of $Bi_{1-x}Sm_xFeO_3$ thin films, including (a)-(d) amplitude, (e)-(h) phase and (i)-(l) phase distribution collections for different *x* value of 0, 0.05, 0.10 and 0.15, respectively.

Piezoelectric performance

PFM scanning techniques are expected to reveal the piezoelectric response and ferroelectric domains orientation.[6, 40, 41] An AC voltage of 3 V was applied on the thin films through the contact between the probe tip and film surface. The out-of-plane (OP) piezoelectric amplitude and phase of $Bi_{1-x}Sm_xFeO_3$ thin films were obtained within an area of 2 μm×2 μm, as shown in Figs. 7(a)-(h), respectively. Phase distribution of each composition was calculated according to the phase mapping results by employing the packaged software of PFM and plotted in Figs. 7(i)-(l). The corresponding topographic images are shown in Figs. 5(a)-(d) and both amplitude and phase show no coupling with the surface topography in any samples.

For *x*=0 and *x*=0.05 films, the OP phase images show two distinguished colours exhibiting perfect 180° contrast and the two regions randomly distribute across the scanned areas. This can be interpreted as the polycrystalline structure in which domains show random orientations. The polarization vectors of domains contain either upward or downward component along the vertical direction of samples, thus leading to 180° contrast.[40, 41] Some regions manifesting high amplitude (yellow region) correspond to domains whose spontaneous polarization direction coincidently lies along the out-of-plane axis. When *x* is increased to 0.10, where *R* and *O* phases coexist, the OP amplitude mapping shows remarkably high piezoelectric responses. The phase distribution presents two peaks with 180° contrast though one of the peaks dominates in area. Generally, the spontaneous polarization directions of *R* phase are <111> with 8 possible polarization variants, while the case of *O* phase are <110> with 12 possible polarization variants.[42, 43] At this composition with phase coexistence, the Gibbs free energy of the two phases is close and multiple polarization variants of domains tend to switch to the direction following the external electric field.[44] Besides, 20 underlying polarization variants give rise to the probability of domain switching thus leading to high piezoelectric response. Phase distribution also confirms that a large amount of domains have been switched. The high piezoelectric performance is also in agreement with literatures that large d_{33} value can be obtained at *R-O* MPB.[9, 11] For the case of *x*=0.15, the OP amplitude becomes smaller and phase image manifests no obvious discrepancy. These features should be ascribed to the weak ferroelectricity the sample possesses which is discussed in the previous part. As the coercive field of the composition is small, domains are supposed to switch completely to the direction along the external electric field.

Since the amplitude of PFM mapping is sometimes dependent on the sample surface condition, the piezoelectric properties of $Bi_{1-x}Sm_xFeO_3$ thin films were further characterized by using local switching spectroscopy piezoresponse force microscopy (SS-PFM) techniques. Different from the PFM scanning mode, in SS-PFM mode a step-varying DC voltage ranging from -30V to 30V was applied to the sample to pole the ferroelectric thin film and a modulated AC voltage of 3V was applied simultaneously to excite surface piezoresponse and to acquire the signal.[45] The acquired piezoresponse manifests hysteresis loops and are plotted in Fig. 8.

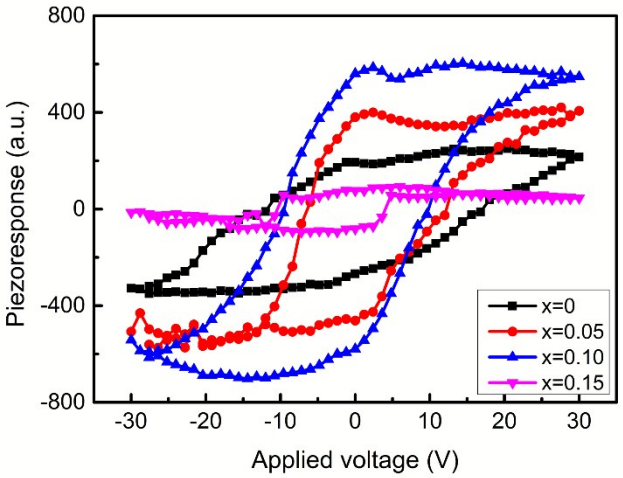

Fig. 8. Piezoresponse of $Bi_{1-x}Sm_xFeO_3$ thin films using local switching spectroscopy PFM test.

We focused on the absolute value of the piezoresponse at the maximum voltage which represents the deformation of sample under a large electric field, under which complete polarization switching was achieved in all four samples. The average piezoresponse value in $Bi_{1-x}Sm_xFeO_3$ (x=0, 0.05, 0.10 and 0.15) films are 272.1, 486.9, 569.4 and 63.3 (a.u.) respectively and correspond to the magnitude of the reverse piezoelectric coefficient. The piezoelectric performance increases with Sm content when x is smaller than 0.10 and then decreases sharply at x=0.15. The asymmetry of hysteresis loops at positive and negative sides is related with the imprint electric field. It might result from defects in films or bad contact between electrode-film interfaces. During the poling process, electronic charges accumulate at the interface and result in a deviation from the applied electric field to the actual one. Besides, the electrostatic charges on the sample surface also gives rise to the non-perfect hysteresis loop, though in the SS-PFM mode, the affection has already been weakened.[46]

From the results obtained so far, one can find that comparing with pure $BiFeO_3$ and $Bi_{0.95}Sm_{0.05}FeO_3$, the thin film at x=0.10 manifests reduced dielectric and ferroelectric properties while its piezoelectric performance improves. P_r is mainly related with the displacement of centres of positive and negative charges of the crystal cell. Due to the smaller radius of Sm^{3+} compared with Bi^{3+}, remnant polarization decreases with Sm content in $BiFeO_3$, accompanied with the phase transition from *R*3*c* to *Pbam* and finally *Pnma*.[11, 12, 14, 17]. It can be concluded that the enhancement of piezoelectricity comes mainly from the extrinsic contribution. That is, domain switching contributes more to the piezoelectricity at x=0.10 than the displacement of centres of positive and negative charges. As for the dielectric property, since it was tested under a low voltage of 0.5 V which is not sufficient to induce the domain switching, though the domain switching can also contribute to the permittivity, the dielectric properties did not show a prominent increase in this sample. The decrease of permittivity can be ascribed to the intrinsic decrease of ferroelectricity and reduction of crystal boundaries as discussed before.

The improved piezoelectric performance can be ascribed to the phase coexistence of *R*3*c* and *Pbam* phases implying a *R-O* MPB. Different from the 14% Sm composition reported in other literatures in which the MPB locates at the phase boundary between *R*3*c*+*Pbam* and *Pnma*, [8,9,11] in our thin films, it locates at the 10% Sm doping content where *R*3*c* and *Pbam* coexist. It can be ascribed to the influence due to the different thermal expansion coefficients between Si (c.a. 2.6×10^{-6} K^{-1}-4.0×10^{-6} K^{-1}) and $BiFeO_3$ (c.a. 6.5×10^{-6} K^{-1}-13×10^{-6} K^{-1}).[2] Crystallization process takes place at a high temperature and no thermal stress generates at this stage. However, after the samples are cooled down, tensile stress comes into being along the in-plane direction of sample $BiFeO_3$ thin films due to the large thermal expansion coefficient difference.[47] According to first principle calculation, tensile stress favours the orthorhombic phase,[44, 48] so lower Sm content is needed to induce the phase transition, compared with $BiFeO_3$ grown epitaxially on $SrTiO_3$ single crystal substrate which contrarily imposes a compressive stress on $BiFeO_3$.[44]

As shown in Fig. 8, the $Bi_{0.85}Sm_{0.15}FeO_3$ film demonstrated a piezoresponse hysteresis loop, but its piezoelectricity is very weak. Since *Pnma* is a centrosymmetric structure displaying no piezoelectricity, the ferroelectricity can be ascribed to the *Pbam* phase as revealed in the XRD refinement. Nevertheless, no evidence of a double loop was found in ferroelectric or piezoelectric test to affirm the existence of the anti-polar *Pbam* phase. The same situation was also found in $Bi_{0.85}Sm_{0.15}FeO_3$ ceramic samples.[22] The observed piezoelectricity may be due to the existence of a small amount of *Pbam* phase as indicated in the refinement. The anti-polar structure of *Pbam* originates from the cooperative displacements of Bi and O atoms along certain direction and the double hysteresis loops were only found in (001) epitaxial thin films.[11, 34] So, it might be difficult to observe the anti-ferroelectric properties in polycrystalline thin films. Besides, at the composition near the phase boundary, the very high electric field applied during SS-PFM test may lead to a phase transition from *Pnma* to *R*3*c* or a more complex phase.[49] Another possibility is phase segregation. Since rare-earth doped $BiFeO_3$ is prone to formation of Bi rich and rare-earth rich region,[50] the tested area in SS-PFM mode might just locate at a Bi rich region belonging to *R*3*c*.

Conclusions

In summary, a series of $Bi_{1-x}Sm_xFeO_3$ thin films (x=0, 0.05, 0.10 and 0.15) was fabricated on the widely used platinized silicon substrates via the sol-gel method. The composition-dependent crystal sizes and film roughness was analyzed by AFM. The Sm^{3+} substitution for Bi^{3+} caused a phase transition from rhombohedral to orthorhombic, mainly since Sm^{3+} has a smaller radius than Bi^{3+}. Furthermore, a potential rhombohedral-orthorhombic MPB at x=0.10 was proposed based on synchrotron radiation X-ray and Raman spectroscopy results and XRD refinement indicates the space groups of the two phases are *R*3*c* and *Pbam*. The MPB position x=0.10 is smaller than the x=0.14 reported in epitaxially grown Sm-doped $BiFeO_3$. This difference may be ascribed to the tensile thermal stress generated from silicon substrates which possess a rather small thermal expansion coefficient, as is favourable to orthorhombic phase.

Moreover, PFM scanning and local SS-PFM test confirmed an enhancement of piezoelectric response at MPB. Combining the ferroelectric tests with PFM analysis, the domain switching mechanism was discussed and associated with the improved piezoelectric performance at MPB.

Acknowledgements

This work was supported by National Nature Science Foundation of China (Grants no. 51332002, 51221291) the Ministry of Science and Technology of China under the Grant 2015CB654605. We thank the SSRF for access to BL14B1 beamline and Prof. Lutterotti for helpful guidance on the use of Maud software.

Notes and references

State Key Laboratory of New Ceramics and Fine Processing, School of Materials Science and Engineering, Tsinghua University, 100084 Beijing, P. R. China. E-mail: jingfeng@mail.tsinghua.edu.cn; Fax: +86-10-62784845; Tel: +86-10-62771160

1 J. Wang, J. B. Neaton, H. Zheng, V. Nagarajan, S. B. Ogale, B. Liu, D. Viehland, V. Vaithyanathan, D. G. Schlom, U. V. Waghmare, N. A. Spaldin, K. M. Rabe, M. Wuttig and R. Ramesh, *Science*, 2003, **299**, 1719.
2 G. Catalan and J. F. Scott, *Adv. Mater.*, 2009, **21**, 2463.
3 Y. Yang, J. Y. Sun, K. Zhu, Y. L. Liu and L. Wan, *J. Appl. Phys.*, 2008, **103**, 093532.
4 R. J. Zeches, M. D. Rossell, J. X. Zhang, A. J. Hatt, Q. He, C. H. Yang, A. Kumar, C. H. Wang, A. Melville, C. Adamo, G. Sheng, Y. H. Chu, J. F. Ihlefeld, R. Erni, C. Ederer, V. Gopalan, L. Q. Chen, D. G. Schlom, N. A. Spaldin, L. W. Martin and R. Ramesh, *Science*, 2009, **326**, 977.
5 D. Mazumdar, V. Shelke, M. Iliev, S. Jesse, A. Kumar, S. V. Kalinin, A. P. Baddorf and A. Gupta, *Nano Lett.*, 2010, **10**, 2555.
6 Q. Yu, J.-F. Li, F.-Y. Zhu and J. Li, *J. Mater. Chem. C*, 2014, **2**, 5836.
7 H.-J. Liu, H.-J. Chen, W.-I. Liang, C.-W. Liang, H.-Y. Lee, S.-J. Lin and Y.-H. Chu, *J. Appl. Phys.*, 2012, **112**, 052002.
8 S. Fujino, M. Murakami, V. Anbusathaiah, S. H. Lim, V. Nagarajan, C. J. Fennie, M. Wuttig, L. Salamanca-Riba and I. Takeuchi, *Appl. Phys. Lett.*, 2008, **92**, 202904.
9 C.-J. Cheng, D. Kan, V. Anbusathaiah, I. Takeuchi and V. Nagarajan, *Appl. Phys. Lett.*, 2010, **97**, 212905.
10 C. J. Cheng, D. Kan, S. H. Lim, W. McKenzie, P. Munroe, L. Salamanca-Riba, R. Withers, I. Takeuchi and V. Nagarajan, *Phys. Rev. B*, 2009, **80**, 014109.
11 D. Kan, V. Anbusathaiah and I. Takeuchi, *Adv. Mater.*, 2011, **23**, 1765.
12 D. Kan, C.-J. Cheng, V. Nagarajan and I. Takeuchi, *J. Appl. Phys.*, 2011, **110**, 014106.
13 D. Kan, C. J. Long, C. Steinmetz, S. E. Lofland and I. Takeuchi, *J. Mater. Res.*, 2012, **27**, 2691.
14 C. H. Yang, D. Kan, I. Takeuchi, V. Nagarajan and J. Seidel, *Phys. Chem. Chem. Phys.*, 2012, **14**, 15953.
15 A. Y. Borisevich, E. A. Eliseev, A. N. Morozovska, C. J. Cheng, J. Y. Lin, Y. H. Chu, D. Kan, I. Takeuchi, V. Nagarajan and S. V. Kalinin, *Nat. Commun.*, 2012, **3**, 775.
16 V. V. Lazenka, M. Lorenz, H. Modarresi, K. Brachwitz, P. Schwinkendorf, T. Böntgen, J. Vanacken, M. Ziese, M. Grundmann and V. V. Moshchalkov, *J. Phys. D: Appl. Phys.*, 2013, **46**, 175006.
17 S. B. Emery, C. J. Cheng, D. Kan, F. J. Rueckert, S. P. Alpay, V. Nagarajan, I. Takeuchi and B. O. Wells, *Appl. Phys. Lett.*, 2010, **97**, 152902.
18 W. Chen, W. Ren, L. You, Y. Yang, Z. Chen, Y. Qi, X. Zou, J. Wang, T. Sritharan, P. Yang, L. Bellaiche and L. Chen, *Appl. Phys. Lett.*, 2011, **99**, 222904.
19 Y.-J. Wu, X.-K. Chen, J. Zhang and X.-J. Chen, *Physica B*, 2013, **411**, 106.
20 Y.-J. Wu, X.-K. Chen, J. Zhang, J. Liu, W.-S. Xiao, Z. Wu and X.-J. Chen, *J. Appl. Phys.*, 2013, **114**, 154110.
21 M. Muneeswaran and N. V. Giridharan, *J. Appl. Phys.*, 2014, **115**, 214109.
22 V. A. Khomchenko, J. A. Paixão, B. F. O. Costa, D. V. Karpinsky, A. L. Kholkin, I. O. Troyanchuk, V. V. Shvartsman, P. Borisov and W. Kleemann, *Cryst. Res. Technol.*, 2011, **46**, 238.
23 S. K. Singh, C. V. Tomy, T. Era, M. Itoh and H. Ishiwara, *J. Appl. Phys.*, 2012, **111**, 102801.
24 N.-X. Huang, L.-F. Zhao, J.-Y. Xu, J.-L. Chen, Y. Zhao, *Chin. Phys. Lett.*, 2010, **27**, 027704.
25 Z. Zhong, Y. Sugiyama and H. Ishiwara, *Jap. J. Appl. Phys.*, 2010, **49**, 041502.
26 D. Hong, S. Yu and J. Cheng, *Curr. Appl. Phys.*, 2011, **11**, S255.
27 T. Y. Kim, N. H. Hong, T. Sugawara, A. T. Raghavender and M. Kurisu, *J. Phys-condens. Mat.*, 2013, **25**, 206003.
28 S. K. Singh, *Thin Solid Films*, 2013, **527**, 126.
29 X. Xu, T. Guoqiang, R. Huijun and X. Ao, *Ceram. Int.*, 2013, **39**, 6223.
30 G. Dong, G. Tan, Y. Luo, W. Liu, H. Ren and A. Xia, *Mater. Lett.*, 2014, **136**, 314.
31 V. Sreenivas Puli, D. Kumar Pradhan, S. Gollapudi, I. Coondoo, N. Panwar, S. Adireddy, D. B. Chrisey and R. S. Katiyar, *J. Magn. Mang. Mater.*, 2014, **369**, 9.
32 Supplementary materials.
33 D. Kan and I. Takeuchi, *J. Appl. Phys.*, 2010, **108**, 014104.
34 D. A. Rusakov, A. M. Abakumov, K. Yamaura, A. A. Belik, G. Van Tendeloo and E. Takayama-Muromachi, *Chem. Mater.*, 2011, **23**, 285.
35 M. V. Abrashev, A. P. Litvinchuk, M. N. Iliev, R. L. Meng, V. N. Popov, V. G. Ivanov, R. A. Chakalov and C. Thomsen, *Phys. Rev. B*, 1999, **59**, 4146.
36 J. M. Jehng and I. E. Wachs, *Chem. Mater.*, 1991, **3**, 100.
37 M. Iliev, M. Abrashev, H.-G. Lee, V. Popov, Y. Sun, C. Thomsen, R. Meng and C. Chu, *Phys. Rev. B*, 1998, **57**, 2872.
38 M. N. Iliev and M. V. Abrashev, *J. Raman Spectrosc.*, 2001, **32**, 805.
39 Q. Zhang, X. Zhu, Y. Xu, H. Gao, Y. Xiao, D. Liang, J. Zhu, J. Zhu and D. Xiao, *J. Alloys. Compd.*, 2013, **546**, 57.
40 A. Gruverman and S. V. Kalinin, *J. Mater. Sci.*, 2006, **41**, 107.
41 E. Soergel, *J. Phys. D: Appl. Phys.*, 2011, **44**, 464003.
42 F. Zavaliche, S. Y. Yang, T. Zhao, Y. H. Chu, M. P. Cruz, C. B. Eom and R. Ramesh, *Phase Transit.*, 2006, **79**, 991.
43 J.-F. Li, K. Wang, F. Y. Zhu, L.-Q. Cheng and F.-Z. Yao, *J. Am. Ceram. Soc*, 2013, **96**, 3677.
44 Z. Chen, Z. Luo, C. Huang, Y. Qi, P. Yang, L. You, C. Hu, T. Wu, J. Wang, C. Gao, T. Sritharan and L. Chen, *Adv. Funct. Mater.*, 2011, **21**, 133.
45 S. Jesse, A. P. Baddorf and S. V. Kalinin, *Appl. Phys. Lett.*, 2006, **88**, 062908.
46 S. Jesse, H. N. Lee and S. V. Kalinin, *Rev. Sci. Instrum.*, 2006, **77**,

073702.
47 Z.-X. Zhu, C. Ruangchalermwong and J.-F. Li, *J. Appl. Phys.*, 2008, **104**, 054107.
48 Y. Y. Liu, L. Yang and J. Y. Li, *J. Appl. Phys.*, 2013, **113**, 183524.
49 B. Xu, D. Wang, J. Íñiguez and L. Bellaiche, *Adv. Funct. Mater.*, doi: 10.1002/adfm.201403811.
50 S. Saxin and C. S. Knee, *Dalton Trans.*, 2011, **40**, 3462-3465.

Graphical Abstract

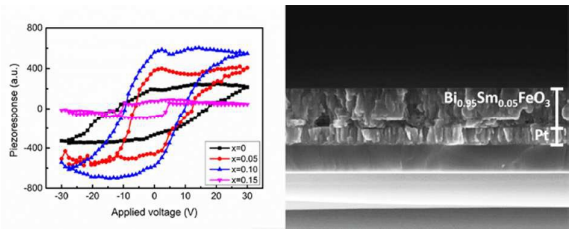

We prepared high-quality $Bi_{1-x}Sm_xFeO_3$ films on Pt(111)/Ti/SiO_2/Si substrates by sol-gel processing and found rhombohedral-orthorhombic phase transition with enhanced piezoelectricity.